arXiv:2302.14187v1 [cond-mat.mes-hall] 27 Feb 2023

Fractal field-effect transistors: Enhanced photodetection and fractal dependent resonances

Bailey Winstanley[1,*] and Alessandro Principi[1,†]

[1] *Department of Physics and Astronomy, University of Manchester, Manchester M13 9PL, UK*

We study gated field effect transistors (FETs) with fractal geometries under Dyakonov and Shur asymmetric boundary conditions, where the source and drain span the left and right edges of the device respectively. An AC THz potential difference is applied between source and gate while a static source-drain voltage, rectified by the nonlinearities of FET electrons, is measured. We find, for a recursion depth, n, that resonant peaks in the potential integrated along the drain at $\omega_n = 3^n\omega_0$ are amplified while all other are diminished. Additionally, we find the presence of peaks with frequencies dependent on the fractal dimensions of both the Sierpinski carpet and a similar alternative fractal. We then show the advantage of employing the alternative fractal as a superior geometry for the photodetector when compared to the Sierpinski carpet.

I. INTRODUCTION

There exists a gap in the frequency spectrum at the low-THz range (between 0.1 and 30 THz) at which there has been an absence of efficient and compact photodetectors and emitters. Known as the "terahertz gap", this gap in the performance of devices operating in the far-infrared region has been an area of interest for some time now [1–3], owing to its contributions to nondestructive imaging, bio-imaging and material spectroscopy [4–7]. One photodetector that has gained traction in this field was predicted in 1996 by Dyakonov and Shur. They posed that a field effect transistor (FET) could be used to generate and detect THz radiation [8–10].

This device consists of a semiconductor quantum-well cavity, hosting a 2D electron gas. The cavity is bounded at one end by a source and by a drain at the other, and is in close proximity to a metal gate. The drain allows no current to flow through, and a THz AC source-gate voltage is applied, this mimics a typical output from THz radiation impinging on an antenna. Along with the asymmetric boundary conditions, we use hydrodynamics to describe the nonlinear flow within the electron fluid. This results in a rectified DC source-drain voltage. This rectification can be thought of as a result of frequency dependant interference between plasmons (collective long wavelength charge density fluctuations [11]) reflected from the drain back to the source. As a result, this rectified potential has peaks at odd multiples of the first bulk plasmon frequency. The device put forth by Dyakanov and Shur has already been experimentally verified in semiconductor quantum wells [12–15] and in graphene-based FETs [16–20]. Furthermore it has been shown that by changing the geometry of the device from Dyakonov and Shur's original square geometry to that of a Corbino disk [21], or even an eccentric Corbino disk [22], the responsivity of the detector can improve. Following these studies we wish to implement a geometry change to the original Dyakonov-Shur (DS) device.

In recent works, the use of fractals in nano-scale heterostructures has been investigated within thermal transport [23 and 24], fractal antennas [25–28], and transducers [29] showing promising results. Fractals are complex structures that at any magnification exhibit self similarity, when employed in fabricated devices they emulate the function of the device at various length scales. Thus for an antenna, a fractal geometry widens the range of accessible frequencies the antenna can receive [28, 30, and 31]. In addition fractals typically allow the reduction in size of devices, leading to both efficient and more cost-effective fabrication, as well as miniaturization applications.

In what follows we apply the Sierpinski carpet to the regular square DS FET. We explain the features of the frequency spectrum that arise from this change in geometry and explore the origins of these features. We show that the splitting of peaks in the nonlinear potential at low frequencies is an inherent property of the geometry, and that the frequency spectrum contains an anomalous peak that lies at a frequency not predicted when considering lengths scales within the device. For comparison, we create a new fractal with an equivalent frequency spectrum, but different anomalous peak frequency. We suggest that this peak arises due to the topology of the fractal geometry, and estimate the possible relationship between the frequency of this peak and the fractal dimension of the geometry. Finally, we compare the use of the Sierpinski carpet fractal to the new fractal outlined in this paper.

II. SIERPINSKI CARPET

The Sierpinski carpet is a plane fractal generated through finite subdivision. This involves recursively dividing a shape into like-subdivisions. For the Sierpinski carpet this recursive algorithm, applied to a square, splits the square into 9 identical sub-squares and removes the centre square. The next level of recursion then applies this algorithm to all remaining sub-squares. Thus by applying this algorithm, we can generate a Sierpinski carpet up to recursion depth, n. Fig.1 illustrates the results of applying this algorithm up to a recursion depth, $n = 3$. At each step of the algorithm the smallest characteristic

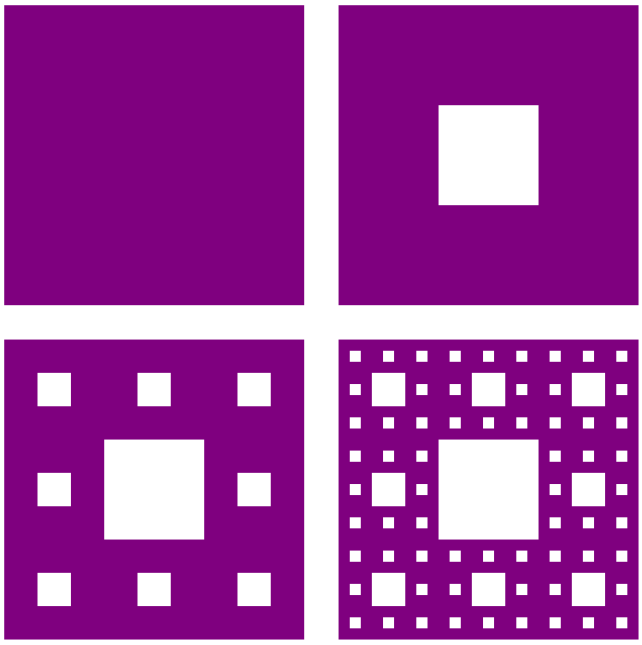


FIG. 1. A diagrammatic representation of the Sierpinski carpet starting at a recursion depth of $n = 0$ (top left) and iterating the recursive algorithm up to $n = 3$ (bottom right).

length scale of the device is reduced by a scaling factor of three, such that for any recursion length, the smallest length scale is $L_n = L/3^n$, where L is the side length of the $n = 0$ square. This fractal, like all others, can be characterised by its fractal dimension (also known as Hausdorff dimension), which for the Sierpinski carpet is $D = \ln N/\ln S = \ln 8/\ln 3 = 1.8928$. For each level of recursion, N is the number of sub-squares the square is divided into, and $1/S$ is the scale factor between the square and sub-squares.

III. HYDRODYNAMIC MODEL

We consider a typical FET geometry. A 2D electron gas is in close proximity to a metal gate, while source and drain electrodes are attached to the left and right edges, respectively. An AC potential is applied between the source and the gate, while the drain allows no current to flow through it. This is simply the DS set up mentioned in their paper [8]. A rectified DC source-drain potential difference is therefore expected, at zero source-drain bias, with peaks in the potential at frequencies, $\omega_{DC} = (2\alpha - 1)\omega_0$, where $\omega_0 = \pi s/2L$ is the lowest resonant frequency and $\alpha \in \mathbb{N}$ counts the resonances. When applied to the Sierpinski carpet for $n > 0$, the system also contains internal edges on which we will apply the drain boundary condition. Our aim is to apply the conditions of the DS model within the outlined fractal regime of the Sierpinski carpet, to determine whether this will result in a useful frequency spectrum or increased gain.

The set of relations that describe our system are the DS relations with altered boundary conditions, and are as follows. The first of these relations is the continuity equation,

$$\partial_t \rho(\boldsymbol{r}, t) + \nabla \cdot [\rho(\boldsymbol{r}, t)\boldsymbol{v}(\boldsymbol{r}, t)] = 0, \tag{1}$$

however, due to the nearby gate we enact the "Local gate approximation":

$$U(\boldsymbol{r}, t) = \rho(\boldsymbol{r}, t)/C \ , \tag{2}$$

and thus the continuity equation becomes

$$\partial_t U(\boldsymbol{r}, t) = -\nabla \cdot [U(\boldsymbol{r}, t)\boldsymbol{v}(\boldsymbol{r}, t)] \ . \tag{3}$$

The second relation takes the form of an Euler equation,

$$\frac{e}{m}\nabla U(\boldsymbol{r}, t) = \partial_t \boldsymbol{v}(\boldsymbol{r}, t) + \frac{1}{\tau}\boldsymbol{v}(\boldsymbol{r}, t) + \nabla v^2(\boldsymbol{r}, t)/2 \ . \tag{4}$$

Here, τ is the average time between two successive collisions with impurities or phonons. We solve the problem posed by the hydrodynamic equations (3)-(4) in conjunction with the usual DS boundary conditions

$$\begin{aligned} U(\boldsymbol{r}, t)|_{\text{source}} &= U_{\text{ext}}(\boldsymbol{r})\cos(\omega t) \ , \\ \hat{\boldsymbol{n}} \cdot \boldsymbol{v}(\boldsymbol{r}, t)|_{\text{drain}} &= 0 \ , \end{aligned} \tag{5}$$

where $\hat{\boldsymbol{n}}$ is the unit vector normal to the drain surface. Unlike in the DS case, the drain here represents both the right edge of the device and all internal edges of the device.

As usual we resort to a perturbative treatment of the system of nonlinear equations. We assume U_{ext} is a small parameter and calculate the rectified nonlinear response as a perturbation to the potential. We then expand $U(\boldsymbol{r}, t)$ and $\boldsymbol{v}(\boldsymbol{r}, t)$ around their equilibrium in the small parameter U_{ext},

$$\begin{aligned} U(\boldsymbol{r}, t) &= U_0 + U_1(\boldsymbol{r}, t) + U_2(\boldsymbol{r}, t) + \mathcal{O}(U_{\text{ext}}^3), \\ \boldsymbol{v}(\boldsymbol{r}, t) &= \boldsymbol{v}_1(\boldsymbol{r}, t) + \boldsymbol{v}_2(\boldsymbol{r}, t) + \mathcal{O}(U_{\text{ext}}^3). \end{aligned} \tag{6}$$

Here $U_0 < 0$ is the equilibrium gate potential (which fixes the charge density in the FET according to $\rho_0 = CU_0$), and the equilibrium velocity, $\boldsymbol{v}_0$, is zero by definition. $U_1(\boldsymbol{r}, t)$ and $\boldsymbol{v}_1(\boldsymbol{r}, t)$, and $U_2(\boldsymbol{r}, t)$ and $\boldsymbol{v}_2(\boldsymbol{r}, t)$ are the linear (order U_{ext}) and nonlinear (order U_{ext}^2) contributions to the potential and velocity, respectively.

Plugging the expansions in Eq. (6) into the set of equations (5)-(10), we collect terms of order U_{ext} and U_{ext}^2 into two systems of differential equations, which are linear in $U_1(\boldsymbol{r}, t)$ and $\boldsymbol{v}_1(\boldsymbol{r}, t)$, and $U_2(\boldsymbol{r}, t)$ and $\boldsymbol{v}_2(\boldsymbol{r}, t)$, respectively. The former pair the linear response of the system and the latter pair yields a rectified nonlinear potential. To focus on the latter part of the potential $U_2(\boldsymbol{r}, t)$, we

average equations over time by integrating over a period of oscillation, $T = 2\pi/\omega$. In this way, the time-dependent parts of $U_2(\boldsymbol{r}, t)$ and $\boldsymbol{v}_2(\boldsymbol{r}, t)$ vanish.

The linear set of equations for $U_1(\boldsymbol{r}, t)$ and $\boldsymbol{v}_1(\boldsymbol{r}, t)$, and $U_2(\boldsymbol{r}, t)$ and $\boldsymbol{v}_2(\boldsymbol{r}, t)$ eventually read

$$\begin{cases} \nabla^2 U_1(\boldsymbol{r}) = -\dfrac{\omega^2 f_\omega}{s^2} U_1(\boldsymbol{r}) \\ U_1(\boldsymbol{r})\Big|_{\text{source}} = U_{\text{ext}}(\boldsymbol{r}) \\ \hat{\boldsymbol{n}} \cdot \nabla U_1(\boldsymbol{r})\Big|_{\text{drain}} = 0 \end{cases} \tag{7}$$

where $s = \sqrt{-eU_0/m}$ is the plasma wave velocity, $f_\omega = 1 + i/(\omega\tau)$, and

$$\begin{cases} \nabla^2 \phi(\boldsymbol{r}) = \dfrac{1}{U_0 \tau} \nabla \cdot [U_1^*(\boldsymbol{r}) \boldsymbol{v}_1(\boldsymbol{r}) + U_1(\boldsymbol{r}) \boldsymbol{v}_1^*(\boldsymbol{r})] \\ \phi(\boldsymbol{r}) - \boldsymbol{v}_1^*(\boldsymbol{r}) \cdot \boldsymbol{v}_1(\boldsymbol{r})\Big|_{\text{source}} = 0 \\ \hat{\boldsymbol{n}} \cdot \nabla \phi(\boldsymbol{r})\Big|_{\text{drain}} = 0 \end{cases} . \tag{8}$$

Here, $\phi(\boldsymbol{r}) = \boldsymbol{v}_1^*(\boldsymbol{r}) \cdot \boldsymbol{v}_1(\boldsymbol{r}) - eU_2(\boldsymbol{r})/m$ and

$$\boldsymbol{v}_1(\boldsymbol{r}) = -\frac{s^2}{U_0} \frac{i \nabla U_1(\boldsymbol{r})}{\omega f_\omega} . \tag{9}$$

The Poisson problem in Eqs. (8) admits a unique solution for $\phi(\boldsymbol{r})$ and therefore for $U_2(\boldsymbol{r}) = m/e\big[\boldsymbol{v}_1^*(\boldsymbol{r}) \cdot \boldsymbol{v}_1(\boldsymbol{r}) - \phi(\boldsymbol{r})\big]$.

IV. RESULTS AND DISCUSSION

We begin with an investigation into the properties of the Sierpinski carpet fractal outlined above with a recursion depth of $n = 1$ (Top right in Fig.1). The nonlinear potential as a function of AC frequency of this geometry within a DS device has been plotted in Fig.2, with comparison to the original DS device, corresponding to $n = 0$. The original DS device has peaks that correspond to $\omega_{\text{DS}} = (2\alpha + 1)\omega_0$. The parameter values chosen in Fig.2 are such that the DS photodetector operates between the regimes of a resonant detector, $s\tau/L \gg 1$, and a broadband detector, $s\tau/L \ll 1$, equivalent to a sub-micrometer device at room temperature [8]. In this regime, with the exception of the lowest frequency peak, all peaks have equivalent magnitude. In comparison, we see that for the $n = 1$ Sierpinski carpet device, resonant frequency peaks in the nonlinear potential corresponding to $\omega_1 = 3\omega_{\text{DS}}$ are magnified, while all other peaks diminish. This occurs due to the removal of the centre square of the DS device. This creates a region with characteristic length scale one third the length of the device, thus the resonant frequencies of this region are three-times larger than those of the original device. Another noticeable feature within the frequency spectrum of the nonlinear potential for $n = 1$ is the splitting of peaks at low frequencies. We expect that these split peaks can be attributed to the diffraction of low energy plasmons within the device, around the missing centre square.

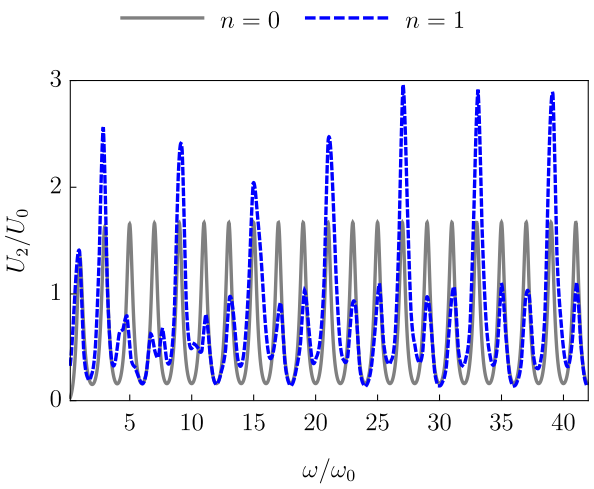


FIG. 2. The nonlinear potential integrated along the drain as a function of frequency, for recursion depths $n = 0, 1$ of the Sierpinski carpet. Both have been plotted for $s\tau/L = 1$ and $\omega_0\tau = 1$.

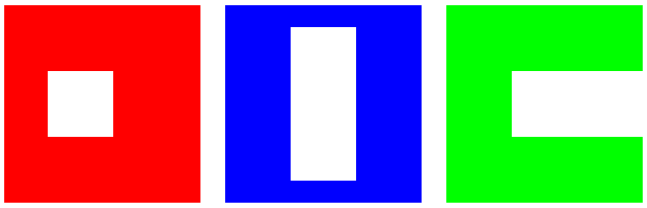


FIG. 3. A diagrammatic representation of three alterations to the $n = 1$ Sierpinski carpet geometry. (Left, red) This consists of shifting the missing centre square towards the source of the device. (Middle, blue) Here the centre square is symmetrically stretched perpendicular to source and drain. (Right, green) In this geometry the absent centre square is stretched all the way to the drain.

To confirm this we modelled a variety of minor geometry changes to the $n = 1$ Sierpinski carpet geometry. By moving the missing centre square closer to the source such as in Fig.3 (left, red) the resonant frequencies that lead to the largest peaks in the potential increase. This is a consequence of decreasing the distance between the source and the removed central sub-square of the device. By symmetrically stretching the centre square perpendicular to the source-drain axis as in Fig.3 (middle, blue), we find that the peaks relating to ω_1 undergo a further amplification while all other are reduced. Finally, we found that by removing the region between the missing centre square and the drain as in Fig.3 (right, green), the nonlinear potential at the drain no longer features

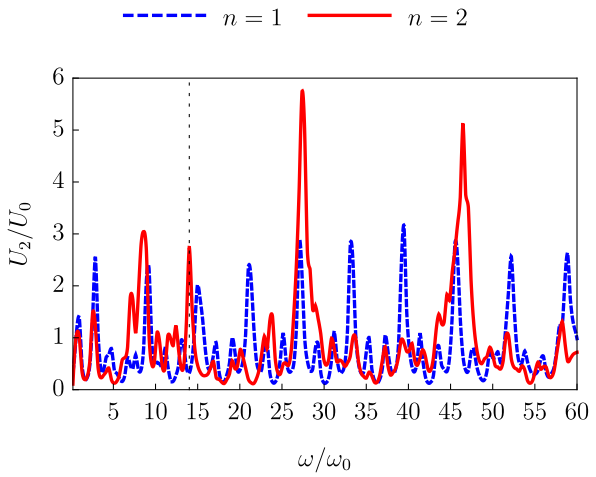


FIG. 4. The nonlinear potential integrated along the drain as a function of frequency, for recursion depths $n = 1, 2$ of the Sierpinski carpet. A large anomalous peak has been marked by the black vertical dotted line at $\omega = 14.01\omega_0$. As in Fig.2, both have been plotted for $s\tau/L = 1$ and $\omega_0\tau = 1$.

peak-splitting at low frequencies, and peak amplitudes became more uniform. The resonant modes of such a device can be thought of as the combination of modes from two DS photodetectors, where one is scaled to a third of the length of the other. More detailed comparisons between the $n = 1$ Sierpinski carpet geometry and those mentioned above can be found in App. A.

Within Fig.4 we compare the already discussed $n = 1$ Sierpinski carpet geometry to the $n = 2$ geometry. As before, the $n = 2$ device features a set of frequency peaks that relate to its smallest characteristic length, which is now $L/9$, while all other frequency peaks shrink. This leads to a set of large-amplitude peaks that lie at the frequencies $\omega_2 = 9\omega_{\mathrm{DS}}$. Additionally we find an anomalous peak that lies at $\omega_a = 14.01\omega_0$. The origin of this peak is unknown, as we believe it too large to be due to the $\alpha = 2$ resonant frequency $\omega_1 = 15\omega_0$. Additionally we find this peak is present in the $n = 3$ geometry, where the peak is located at $3\omega_a$ (see App. B).

To investigate whether the origin of this anomalous peak lies in the geometry's fractality we construct a Sierpinski carpet-like fractal to compare against. This fractal, depicted in Fig.5 is constructed in the same way as the Sierpinski carpet, however in addition to removing the centre square, we also remove the square right of the centre. In this way the dimension of this fractal, $D = \ln 7/\ln 3 = 1.7712$, differs from the Sierpinski carpet. However, as discussed previously, these changes produce the same resonant frequencies as the Sierpinski carpet. For this new fractal the frequency spectrums for recursion depths, $n = 1, 2$, are plotted in Fig.6. Surprisingly, although the anomalous peak is present in the new fractal geometry, it changes frequency to $\omega_b = 13.69\omega_0$.

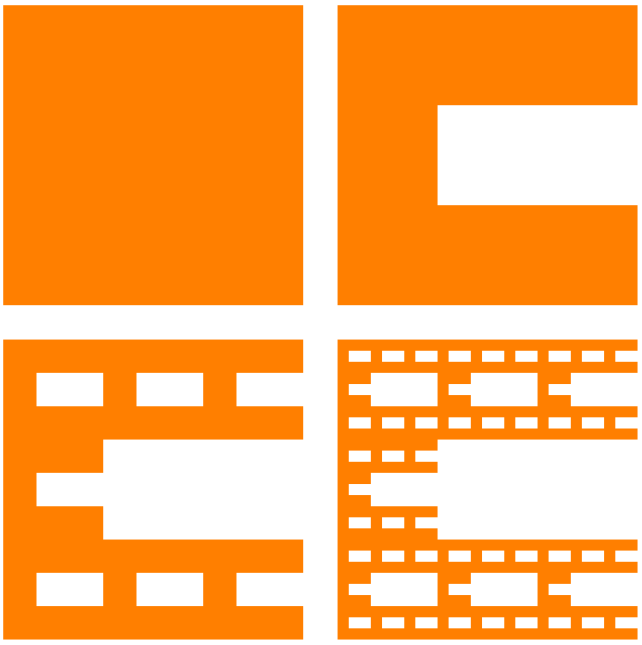


FIG. 5. A diagrammatic representation of the Sierpinski carpet-like fractal up to recursion depth $n = 3$. When generating this fractal, unlike the Sierpinski carpet, both the centre square and the square to the right of the centre are removed.

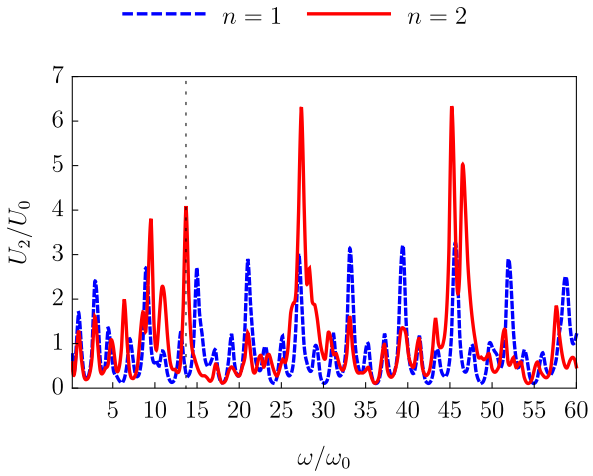


FIG. 6. The nonlinear potential integrated along the drain as a function of frequency, for recursion depths $n = 1, 2$ of the fractal introduced in Fig.5. A large anomalous peak has been marked by the black vertical dotted line at $\omega = 13.69\omega_0$. Parameters are the same as in Fig.4.

We note that the frequency of these anomalous peaks in both fractals are stable against changes to the to the collision time, τ. This suggests that this resonant mode may be topological, and thus be dependant on an inherent property of the geometry such as fractal dimension. While we have insufficient data to empirically state the

form of this function, a reasonable approximation that matches the data we do have is,

$$\omega_{n,D} \approx 3^n \alpha \frac{D^2}{\ln D} \omega_0, \tag{10}$$

where α is a device dependant parameter that is independent of fractal dimension or recursion depth. This predicts both anomalous peaks to three decimal places. While this Sierpinski carpet-like fractal proves useful as a comparative tool, it also serves to improve upon the Sierpinski carpet for use in this photodetector. Not only is there less splitting of peaks present at low frequencies due to diffraction, the resonant peaks in the nonlinear potential for the Sierpinski carpet-like fractal are larger and have more consistent amplitudes at higher frequencies.

V. CONCLUSIONS

In this paper we have studied the application of fractal geometries to a photodetectors that operate by rectifying an AC signal from an external antenna as outlined by Dyakonov and Shur [8]. We model the device with a Sierpinski carpet geometry, up to a recursion depth of $n = 2$, and analyse the features of the nonlinear potential integrated along the drain. We find that for frequencies $\omega_n = 3^n \omega_{DS}$ peaks in the potential are amplified, while all other resonant peaks of the device are suppressed. Additionally we observe the splitting of suppressed peaks at low frequencies. A unique feature we find in the $n = 2$ geometry is an anomalous peak that does not conform to simple length considerations.

To study this anomalous peak we design a new fractal pattern shown in Fig.5. We compare the anomalous peaks present in the nonlinear potentials for these two fractal geometries. We find that in both cases the peaks are robust against changes in the collision time, τ, and present for higher recursion depths. Thus, we conclude that the peaks are due to the device topology and provide a possible formula to predict anomalous peak frequencies with these geometries.

Although the designed fractal pattern in Fig.5 has been used to analyse the anomalous peak present in the Sierpinski carpets frequency spectrum, we suggest the fractal presented here as an alternative to the application of the Sierpinski carpet within DS photodetectors. Compared to the Sierpinski carpet, this fractal results in a greater amplification of ω_n peaks, without the presence of split peaks at low frequencies.

Like for antennas, we show that for a DS photodetector fractals can be applied to select for and amplify specific frequencies, dependant on the size of the device. We predict the presence of a resonant mode of operation that depends on the fractal dimension of the device's geometry. Finally, we present an alternative fractal to the Sierpinski carpet that improves upon the features of the Sierpinski carpet when used as the geometry for a DS photodetector.

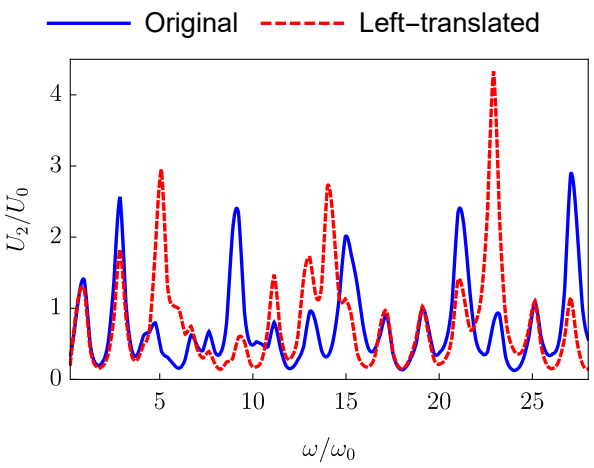


FIG. 7. The nonlinear potential integrated along the drain as a function of frequency, for the Sierpinski carpet fractal geometry with recursion depth $n = 1$ (original) and the altered geometry in Fig.3 (left,red) where the empty centre sub-square is translated $L/9$ to the left.

Appendix A: Geometric changes to the $n = 1$ Sierpinski Carpet

In order to explain the phenomena that occurs in the frequency spectrum of the nonlinear potential within the $n = 1$ Sierpinski carpet, we explore how deviating from the $n = 1$ geometry affects the spectrum. All changes to the potential caused changes in the geometry are compared to the potential of the $n = 1$ Sierpinski Carpet geometry shown in Fig.1.

1. Translating the centre sub-square toward the source

An example of the translation of the removed central sub-square of the $n = 1$ Sierpinski Carpet geometry toward the source is depicted in Fig.3 (left,red). The subsequent change to the nonlinear potential for this geometry employed within the DS photodetector is plotted in Fig.7 with comparison to the original $n = 1$ Sierpinski carpet geometry. We observe that this geometry causes an increase to the largest resonant modes within the device when compared to the original $n = 1$ geometry. This is a result of the reduction of the smallest characteristic length within the device from $L/3$ to $2L/9$. The resonant modes are therefore located at $\omega_{\text{left}} = 9\omega_{\text{DS}}/2$ instead of $\omega_1 = 3\omega_{\text{DS}}$.

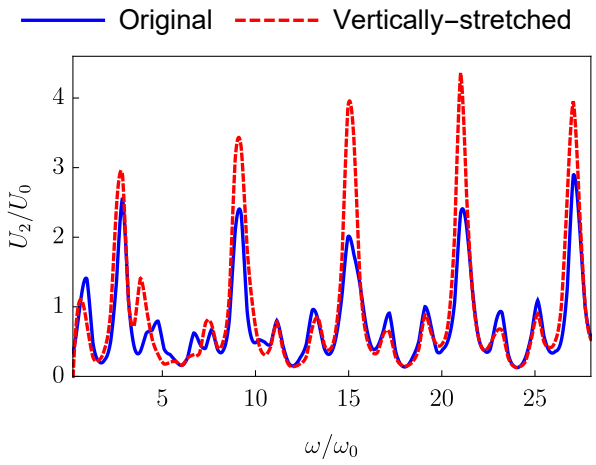


FIG. 8. The nonlinear potential integrated along the drain as a function of frequency, for the Sierpinski carpet fractal geometry with recursion depth $n = 1$ (original) and the altered geometry in Fig.3 (middle, blue) where the empty centre sub-square is symmetrically stretched from $L/3$ to $7L/9$ vertically.

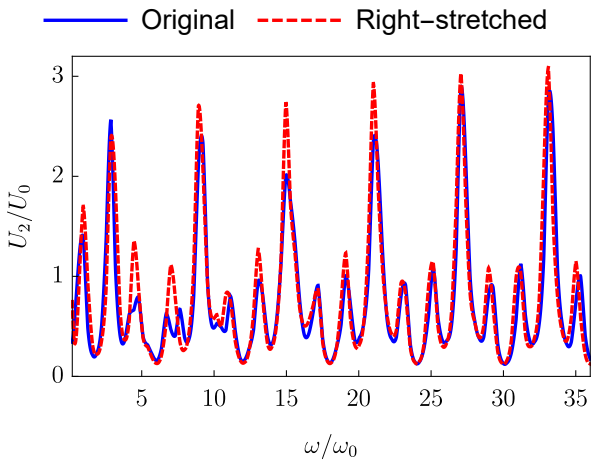


FIG. 9. The nonlinear potential integrated along the drain as a function of frequency, for the Sierpinski carpet fractal geometry with recursion depth $n = 1$ (original) and the altered geometry in Fig.3 (right, green) where the empty centre sub-square is stretched to the right edge.

2. Stretching the central sub-square symmetrically perpendicular to source and drain

By symmetrically stretching the center square perpendicular to the source and drain, depicted in Fig.3 (middle, blue), we expect to see no or little difference in the positioning of peaks within the frequency spectrum as the distance between the source and central sub-square is preserved. We find, illustrated in Fig. 8, that our expectations are confirmed. Additionally, we find that this change in geometry results in large amplitudes for the ω_1 resonance peaks. This is understandable, as the portion of the device devoted to generating plasmons of these frequencies has been increased in size relative to the original $n = 1$ Sierpinski carpet geometry.

3. Expanding the centre sub-square toward the drain

Here we investigate the stretching of the hollow centre sub-square toward the drain depicted in Fig.3 (right, green). Given that the plasmons occur due to the AC source and propagate throughout the FET, it is expected that by expanding the hollow square toward the drain, these plasmons will be minimally affected. The resulting nonlinear potential for this geometry is illustrated in Fig. 9, where we find that while the resonant frequencies within the device remain the same, nearly all resonant peaks of the nonlinear potential are enhanced. In addition their amplitudes are more consistent. One may also observe that for low frequencies, the splitting of peaks that occurs for the $n = 1$ Sierpinski carpet geometry is no longer present for the adapted geometry. From this

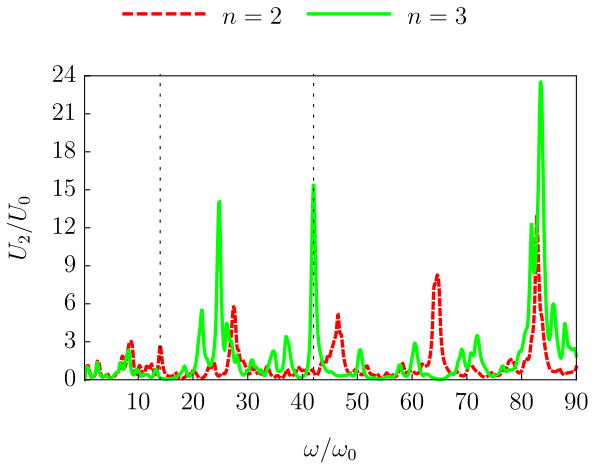


FIG. 10. The nonlinear potential integrated along the drain as a function of frequency, for recursion depths $n = 2, 3$ of the Sierpinski carpet. Large anomalous peaks have been marked by black vertical dotted lines at $\omega = 14.01\omega_0$ for $n = 2$ and $\omega = 42.02\omega_0$ for $n = 3$. Parameters are the same as in Fig.4.

we conclude that the peak splitting must be due to the diffraction of plasmons around the hollow centre of the $n = 1$ Sierpinski carpet geometry.

Appendix B: Sierpinski Carpet nonlinear potential frequency spectrum for $n = 3$

Here we investigate the effect of employing the Sierpinski carpet geometry up to recursion depth $n = 3$ within

a DS photodetector. The frequency dependence of the nonlinear potential integrated across the drain of the device is plotted in Fig.10. As with the transition from the $n = 1$ to the $n = 2$ geometries seen in Fig.4, the frequencies of the largest resonant modes grow by a factor of three and grow in amplitude, while all other resonant modes diminish. Of more interest is the continued presence of an anomalous mode at a frequency precisely three times larger than the $n = 2$ anomalous mode $\omega_a 2 = 3\omega_a$. The sustained presence of this mode at higher recursion depths provides evidence to suggest that the anomalous peaks aren't simply defects of the model, but instead unique to this fractal geometry.

* bailey.winstanley@manchester.ac.uk
† alessandro.principi@manchester.ac.uk

[1] A. Grigorenko, M. Polini, and K. Novoselov, Nature Photon **6**, 749–758 (2012).
[2] F. Bonaccorso, Z. Sun, T. Hasan, and A. C. Ferrari, Nature Photonics **4**, 611–622 (2010).
[3] M. Tonouchi, Nature photonics **1**, 97 (2007).
[4] R. Kleiner, Science **318**, 1254 (2007).
[5] P. Alonso-González, A. Nikitin, Y. Gao, A. Woessner, M. Lundeberg, A. Principi, N. Forcellini, W. Yan, S. Vélez, A. Huber, K. Watanabe, T. Taniguchi, F. Casanova, L. Hueso, M. Polini, J. Hone, F. Koppens, and R. Hillenbrand, Nature nanotechnology **12**, 31 (2016).
[6] X. Deng, L. Li, M. Enomoto, and Y. Kawano, Scientific Reports **9**, 3498 (2019).
[7] X. Fu, Y. Liu, Q. Chen, Y. Fu, and T. J. Cui, Frontiers in Physics **10** (2022), 10.3389/fphy.2022.869537.
[8] M. Dyakonov and M. Shur, IEEE Transactions on Electron Devices **43**, 380 (1996).
[9] M. I. Dyakonov and M. S. Shur, Applied Physics Letters **67**, 1137 (1995).
[10] M. I. Dyakonov and M. S. Shur, Phys. Rev. B **51**, 14341 (1995).
[11] G. Giuliani and G. Vignale, *Quantum Theory of the Electron Liquid* (Cambridge University Press, 2005).
[12] W. Knap, J. Lusakowski, T. Parenty, S. Bollaert, A. Cappy, V. V. Popov, and M. S. Shur, Applied Physics Letters **84**, 2331 (2004).
[13] N. Dyakonova, A. El Fatimy, J. Łusakowski, W. Knap, M. I. Dyakonov, M.-A. Poisson, E. Morvan, S. Bollaert, A. Shchepetov, Y. Roelens, C. Gaquiere, D. Theron, and A. Cappy, Applied Physics Letters **88**, 141906 (2006).
[14] S. Kang, P. J. Burke, L. N. Pfeiffer, and K. W. West, Applied Physics Letters **89**, 213512 (2006).
[15] W. Knap, M. Dyakonov, D. Coquillat, F. Teppe, N. Dyakanova, J. Lusakowski, K. Karpierz, M. Sakowicz, G. Valusis, D. Seliuta, I. Kasalynas, A. E. Fatimy, Y. M. Meziani, and T. Otsuji, J Infrared Milli Terahz Waves **30**, 1319 (2009).
[16] A. Tomadin and M. Polini, Phys. Rev. B **88**, 205426 (2013).
[17] H. Yan, Z. Li, X. Li, W. Zhu, P. Avouris, and F. Xia, Nano Letters **12**, 3766 (2012).
[18] L. Vicarelli, M. S. Vitiello, D. Coquillat, A. Lombardo, A. C. Ferrari, W. Knap, M. Polini, V. Pellegrini, and A. Tredicucci, Nature Materials **11**, 865–871 (2012).
[19] A. Principi, D. Bandurin, H. Rostami, and M. Polini, Phys. Rev. B **99**, 075410 (2019).
[20] F. Koppens, T. Mueller, P. Avouris, A. Ferrari, M. Vitiello, and M. Polini, Nature nanotechnology **9**, 14 (2014).
[21] M. Khavronin, A. Petrov, A. Kazantsev, E. Nikulin, and D. Bandurin, Phys. Rev. Applied **13**, 064072 (2020).
[22] B. Winstanley, H. Schomerus, and A. Principi, Phys. Rev. B **104**, 165406 (2021).
[23] Y. Kang, F. Duan, S. Shangguan, Y. Zhang, T. Zhou, and B. Si, Molecules **23** (2018), 10.3390/molecules23123294.
[24] A. Krishnamoorthy, N. Baradwaj, A. Nakano, R. Kalia, and P. Vashishta, Scientific Reports **11** (2021), 10.1038/s41598-021-81055-4.
[25] F. De Nicola, N. S. P P, D. Spirito, M. Miscuglio, F. Tantussi, A. Tomadin, F. Angelis, M. Polini, R. Krahne, and V. Pellegrini, ACS Photonics **5** (2018), 10.1021/acsphotonics.8b00186.
[26] K. Tiwari, A. Yadav, R. Chawhan, and D. Singha, JOURNAL OF TELECOMMUNICATIONS **8**, 73 (2011).
[27] R. Mohanamurali and T. Shanmuganantham, International Journal of Computer Applications **39**, 19 (2012).
[28] R. Gurjar, D. K. Upadhyay, B. K. Kanaujia, and A. Kumar, AEU - International Journal of Electronics and Communications **117**, 153126 (2020).
[29] S. Canning, A. Walker, and P. Roach, Fractals **25**, 1750050 (2017).
[30] K. Vinoy, J. Abraham, and V. Varadan, IEEE Transactions on Antennas and Propagation **51**, 2296 (2003).
[31] J. Jayasinghe, A. Andújar, and J. Anguera, Microwave and Optical Technology Letters **61**, 772 (2019), https://onlinelibrary.wiley.com/doi/pdf/10.1002/mop.31605.